

A Systematic Study to Improve the Performance of SrCoO_3 as an Anion-Intercalation-Type Electrode for Supercapacitors Through Interface, Oxygen Vacancies, and Doping

Sadhana Lolla and Xuan Luo

National Graphene Research and Development Center, Springfield, VA, 22151, USA

(Dated: February 19, 2024)

Abstract

Supercapacitors have recently gained popularity as possible energy storage systems due to their high cycling ability and increased power density. However, one of the major drawbacks of supercapacitors is that they have a low energy density, which makes them less effective than batteries. Herein, we explore different methods of increasing the supercapacitor performance of the perovskite SrCoO_3 . We carry out first-principles calculations to systematically study how SrCoO_3 /graphene interface, oxygen vacancies, and doping improve the performance of strontium cobaltite as an anion-intercalation-type supercapacitor. The results show that the SrCoO_3 /graphene interface is relatively stable with a formation energy of 1.3 eV and is highly conductive, which makes it a promising material for supercapacitors. We also find that inducing oxygen vacancies in SrCoO_3 significantly increases the conductivity of this material. Results of doping calculations reveal that doping with Mo, V, P, and Nb all increase the stability and conductivity of SrCoO_3 . We find that niobium is the most stable and most conductive of all four dopants. In addition, we find that vanadium is a very promising novel dopant for SrCoO_3 as an anion-intercalation-type supercapacitor electrode material.

I. INTRODUCTION

Global warming is wreaking destruction on habitats around the world, polluting the air and water, and putting endangered species at risk. In light of this growing environmental crisis, renewable energy sources such as wind, solar, and hydrothermal energy are becoming crucial to the growth of sustainable clean energy¹. In addition, over the past decade, concerns regarding environmental health have propelled the movement away from traditional gasoline-powered vehicles to more environmentally friendly such as electric vehicles (EVs) and hybrid electric vehicles (HEVs). However, both clean energy sources and EVs require fast and powerful energy storage devices². Supercapacitors have the potential to fill this need due to their unique properties and widespread applications³.

Though the first patent for a supercapacitor was filed in 1957⁴, supercapacitors have only recently begun to attract widespread interest because of their fast charge-discharge rate, high power density, and long cycle life⁵. However, there are two main disadvantages facing the development of supercapacitors: they have high production costs and low energy densities (ED), which make them less effective than lithium ion batteries. The types of supercapacitors include traditional electric double layer capacitors (EDLCs) and pseudocapacitors. Of these two types, pseudocapacitors are generally preferred because they have a higher ED than EDLCs due to the reversible redox reactions between electrode materials and electrolytes⁶. However, the ED of pseudocapacitors still does not match the ED of batteries. Therefore, one popular method of improving supercapacitor performance has been to develop new electrode materials for pseudocapacitors. Materials used in pseudocapacitors include transition metal oxides (TMOs)^{7–12}, which have been extensively researched for this purpose. TMOs, specifically ruthenium oxide, are widely regarded as some of the most promising materials for pseudocapacitors⁴. However, ruthenium is an extremely expensive material and therefore electrodes made of ruthenium are not desirable. Recently, a third type of supercapacitor electrode has been proposed based on anion-intercalation mechanisms. These anion-intercalated electrode materials often produce higher energy densities than either pseudocapacitors or EDLCs because electrode reactions in the intercalation-type supercapacitors are similar to those in lithium-ion batteries¹³.

Perovskite oxides of the form ABO_3 have the potential to be extremely effective anion-intercalation-type supercapacitor electrode materials due to their natural oxygen vacancies

and defects¹⁴, which make them extremely conductive and give them the potential for both high energy density¹⁵ and high power density. Preliminary experimental studies have demonstrated high cycling ability and promising energy densities^{16–18} of ABO_3 as a supercapacitor electrode.

Perovskite/graphene composites have the potential to further improve the energy density for supercapacitor applications, as graphene can enhance the conductivity of the perovskite oxide and the cluster structure of the perovskite can effectively reduce the agglomeration of graphene¹⁷. In addition, inducing oxygen vacancies in perovskite oxides can improve their performance as anion-intercalation-type supercapacitor electrodes. Furthermore, doping the perovskite oxide at the B-site increases the stability and conductivity of the complex, especially of cubic perovskite oxides^{15,18,19}. However, we are currently unaware of studies that have focused on perovskite oxides combined with graphene for supercapacitor applications. Therefore, our objective is to determine whether the performance of perovskite oxides can be improved through various methods in order to increase the energy density and/or power density of supercapacitors.

We choose SrCoO_3 as our perovskite oxide because of its high Oxygen Evolution Rate (OER)²⁰ and its behavior as an extremely active catalyst²¹, which means that oxygen vacancies can be created very easily in this material. Using first-principles calculations, we explore the conductivity and stability of an SrCoO_3 /graphene interface. We also induce oxygen vacancies in SrCoO_3 to observe their effect on the conductivity of the perovskite for supercapacitor applications. In addition, we conduct doping calculations with Mo, V, P, and Nb to determine which dopant is the most effective in terms of conductivity and stability. We calculate band structure, DOS, and formation energy for all of the compounds.

The rest of this paper is structured as follows: first, we will discuss the computational methods and material selection process and we will then discuss the results of our DFT calculations and their impact on the field of supercapacitors as a whole.

TABLE I: Electronic Configuration and PAW radius cutoff used to generate PAW pseudopotentials

Element	Electronic Configuration (core/val)	PAW radius cutoff (a.u.)
Strontium	[Ar $3d^{10}$] $4s^2 4p^6 5s^1 4d^1$	2.2
Cobalt	[Ne] $3s^2 3p^6 4s^1 3d^8$	2.1
Oxygen	[He] $2s^2 2p^4$	1.4
Carbon	[He] $2s^2 2p^2$	1.5
Molybdenum	[Ar $3d^{10}$] $4s^2 4p^6 5s^1 4d^5$	2.2
Phosphorus	[Ne] $3s^2 3p^3$	1.9
Niobium	[Ar] $3d^{10} 4s^2 4p^6 5s^1 4d^4$	1.4

II. METHODS

A. Computational Methods

All first-principle density functional theory (DFT) calculations were conducted using ABINIT²². The Generalized Gradient Approximation (GGA) and the Perdew-Burke-Ernzerhof (PBE)²³ exchange-correlation functionals were utilized to determine the electronic structure properties of various materials. The pseudopotentials were based on the Projector Augmented Wave (PAW)²⁴ method and the projectors were generated using AtomPAW²⁵.

B. Convergence

The kinetic energy cutoff and Monkhorst-Pack k-point grids were converged for all materials. The self-consistent field (SCF) total energy tolerance was set as 1.0×10^{-10} Ha. Once this tolerance was reached twice consecutively, the SCF iterations were terminated. The kinetic energy cutoff and Monkhorst-Pack k-point grids were considered converged when the differences in total energies were less than 1.0×10^{-4} Ha (about 3 meV) twice consecutively. The converged values for all materials can be found in Table II.

TABLE II: Converged values of the kinetic energy cutoff and Monkhorst-Pack k-point grids for each material.

Material	Energy Cutoff (Ha)	k-mesh
SrCoO ₃	20	$4 \times 4 \times 4$
Graphene	19	$4 \times 4 \times 1$
Mo	13	$6 \times 6 \times 6$
P	23	$8 \times 8 \times 8$
Nb	17	$6 \times 6 \times 6$
V	13	$6 \times 6 \times 6$

C. Relaxation

The converged values for the kinetic energy cutoff and k-mesh were used to fully relax all systems studied. All structures were relaxed using the Broyden–Fletcher–Goldfarb–Shanno algorithm. The SCF iterations were terminated when the Hellman-Feynman forces were less than 5.0×10^{-6} Ha/Bohr twice consecutively. Structures were considered fully relaxed when the maximal force was less than 5×10^{-5} Ha/Bohr.

D. Materials

When used in supercapacitor applications, perovskite oxides usually follow the structure ABO₃. We choose SrCoO₃ as our perovskite because of its high OER²⁰. Other theoretical studies have also predicted that strontium cobaltite has the highest OER ability among all perovskites through DFT calculations²¹. This makes SrCoO₃ a good candidate for supercapacitors because oxygen vacancies increase conductivity, especially in anion-intercalation supercapacitors²⁶.

The cubic structure of the perovskite SrCoO₃ was chosen as the base material for all calculations due to its high conductivity.

1. *Interface*

Experimental studies have speculated that graphene has the potential to increase the stability conductivity of perovskite oxides¹⁷. However, we are unaware of any experimental or theoretical studies to date that have focused on the effects of graphene on perovskite oxides for supercapacitor applications. In this study, we simulate an interface by combining an SrCoO₃ supercell with graphene. To do this, the kinetic energy cutoff was calculated for both pristine SrCoO₃ and pure graphene and the larger of the two was used for interface calculations. These values can be found in Table II. The relaxed lattice constant for SrCoO₃ was chosen for the interface in order to best analyze the effects of graphene on strontium cobaltite. To obtain the layer-by-layer distance d between SrCoO₃ and graphene, we systematically increase d in increments of 0.5 Bohr and compare the total energy. The layer-by-layer distance with the lowest total energy is used in band structure and PDOS calculations.

2. *Oxygen Vacancy*

Numerous studies have demonstrated that oxygen vacancies improve the conductivity of compounds in supercapacitor applications^{8,27,28}. This is especially true for perovskites of the form ABO₃ where B is a transition metal because oxygen vacancies change the geometric and chemical properties⁸ of TMOs. To the best of our knowledge, oxygen vacancies have not been theoretically studied in perovskite oxides for supercapacitor applications. In the present study, we induce oxygen vacancies in strontium cobaltite to determine the mechanism by which vacancies improve the conductivity of this perovskite oxide. We simulated one oxygen vacancy in a $2 \times 2 \times 1$ supercell by removing an oxygen. This structure was then relaxed and the band structure, PDOS, and formation energy were calculated.

Two oxygen vacancies were created by taking out an oxygen and its nearest neighbor. The structure was fully relaxed again and the above procedures were repeated for the complex with two vacancies.

3. Doping

We choose four different dopants for SrCoO_3 : Mo, V, P, and Nb because they have been shown to increase the OER of SrCoO_3 and other similar perovskites. Substitutional doping of 25% was achieved at the B-site by replacing one cobalt with a dopant in a $2 \times 2 \times 1$ supercell. The kinetic energy cutoff was calculated for each dopant and for pristine SrCoO_3 and the maximum of the two was chosen for the doping calculations. These values are displayed in Table II. Previous experimental studies have explored Mo and Nb as dopants for SrCoO_3 as an anion-intercalation-type supercapacitor and concluded that both Mo and Nb increase the conductivity of strontium cobaltite^{5,29}. We use Mo and Nb as dopants in this study to examine how they improve the performance of SrCoO_3 as an electrode material for anion-intercalation-type supercapacitors. P-doped SrCoO_3 has previously been studied as a water oxidation electrocatalyst and has been shown to increase the OER of SrCoO_3 ¹⁵. We use phosphorus as a dopant to determine whether phosphorus can be as effective as the other metallic dopants for SrCoO_3 . Vanadium-doped transition metal oxides have been explored as possible electrode materials³⁰ for pseudocapacitors. In this study, we analyze the conductivity and stability of the V-doped SrCoO_3 to determine if it is also an effective dopant for perovskite oxides for anion-intercalation-type supercapacitors.

E. Band Structure

Using the cubic atomic structure of SrCoO_3 shown in Figure 1 (a), the band structure was calculated for the interface, vacancy, and doping calculations. To transform the lattice vectors a_1 , a_2 , and a_3 into the reciprocal space lattice vectors b_1 , b_2 , and b_3 , Eqs. (1)-(3) were used. High symmetry k-points were then selected to comprehensively sample the first Brillouin zone. For doping and vacancy calculations, the high symmetry k-points for simple cubic structures were chosen and are: Γ (0, 0, 0), X(0, 0.5, 0), M(0.5, 0.5, 0.0), and R(0.5, 0.5, 0.5). The first Brillouin zone and high symmetry k-points for simple cubic structures are shown in Figure 1 (b). When plotting the band structures, each band contained two electrons and four additional conduction bands were used.

Likewise, the band structure was also calculated for pure hexagonal monolayer graphene, which is shown in Figure 1(c). Eqs. (1)-(3) were used to transform the lat-

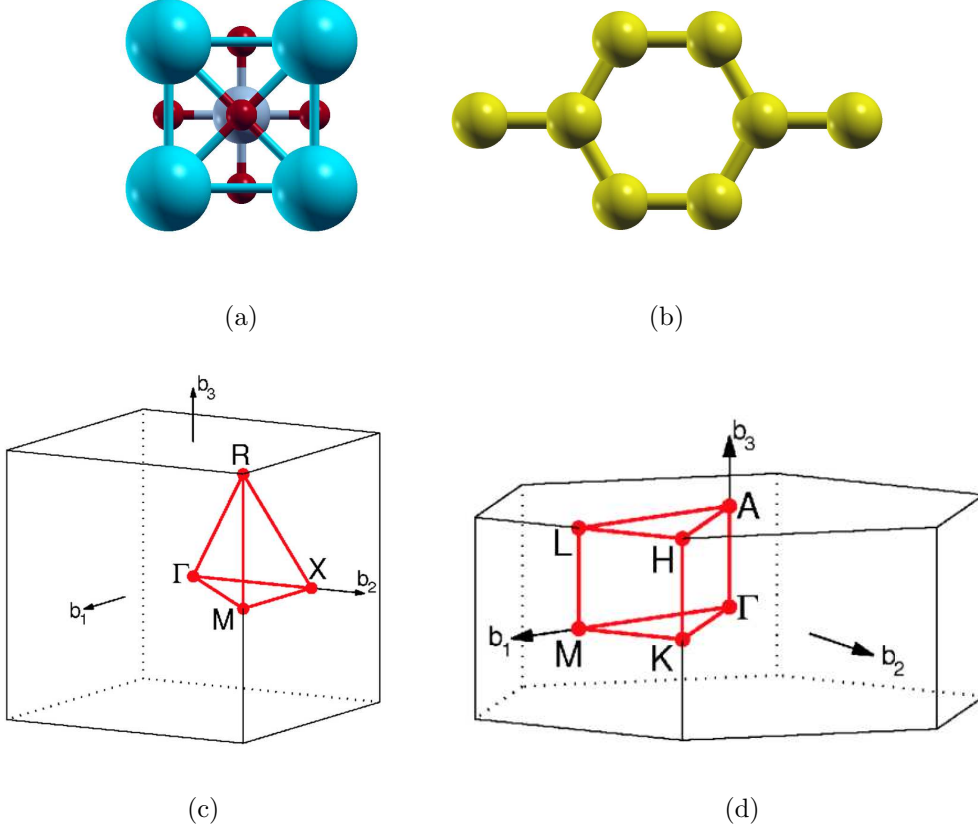


FIG. 1: (a) Aerial view of SrCoO₃ simple cubic crystal structure. (b) Aerial view of hexagonal monolayer graphene. (c) Simple cubic high symmetry k-points³¹. (d) Hexagonal high symmetry-kpoints in the first Brillouin zone³¹.

tice vectors into the reciprocal space lattice vectors, and the high symmetry k-points for hexagonal structures were used: Γ (0, 0, 0), $K(1/3, 2/3, 0)$, and $M(0, 0, 0)$. Figure 1(d) shows the first Brillouin zone and hexagonal high symmetry k-points.

We plotted the fat-band structures for the doped complex structures to analyze the contributions of dopants to the overall band structure of the compound. Similarly, we also calculate the fat-band structures for SrCoO₃ with oxygen vacancies to study the contributions of the Oxygen 2p orbital to the band structure of the complex.

$$\vec{b}_1 = 2\pi \frac{\vec{a}_2 \times \vec{a}_3}{\vec{a}_1 \cdot (\vec{a}_2 \times \vec{a}_3)} \quad (1)$$

$$\vec{b}_2 = 2\pi \frac{\vec{a}_3 \times \vec{a}_1}{\vec{a}_2 \cdot (\vec{a}_3 \times \vec{a}_1)} \quad (2)$$

$$\vec{b}_3 = 2\pi \frac{\vec{a}_1 \times \vec{a}_2}{\vec{a}_3 \cdot (\vec{a}_1 \times \vec{a}_2)} \quad (3)$$

F. Density Of States

Total DOS (TDOS) and projected DOS (PDOS) were calculated for the SrCoO₃/graphene interface, oxygen vacancy, and doping complex systems. The TDOS was used to analyze the overall conductivity of the complex and the PDOS was analyzed to find the contributions of each orbital to the conduction process. We plot the PDOS of the 3*d* orbital for Sr, the 3*d* orbital for Co, the 2*p* orbital for Oxygen, and the *d* orbitals for all the dopants except Phosphorus, which lacks a *d* orbital, so the *p* orbital was used instead.

G. Charge Transfer/Density

We calculate the charge density for structures with oxygen vacancies in order to determine where the charge accumulates after the vacancy is induced. To do this, the converged charge density of the complex structure was obtained by calculating the total energy using the converged values for the kinetic energy cutoff and Monkhorst-Pack k-point grids along with the relaxed lattice constants. This total energy calculation is then used to generate isosurface diagrams for both one vacancy and two vacancy calculations.

We also calculate the charge transfer for the SrCoO₃/graphene interface using the formalism in Eq. (4). To calculate the charge transfer, the converged charge density was obtained through the total energy calculation. The total energy is calculated using the converged kinetic energy cutoff, Monkhorst-Pack k-point grids, and layer-by-layer distance *d*. The charge density of pristine SrCoO₃ and pure graphene are subtracted from the charge density of the interface to determine the electrons gained or lost. The red regions in the isosurface diagrams represent the charge accumulation and the blue regions represent the charge depletion.

$$Q_{transfer} = Q_{interface} - Q_{SrCoO3} - Q_{graphene} \quad (4)$$

H. Formation energy

The formation energies for doping, oxygen vacancy, and interface complex systems were calculated. A lower formation energy indicates a more stable compound, and a negative formation energy is preferred because it indicates that an exothermic reaction has occurred. The formation energy for all complex systems were calculated using Eq. (5), where E_f represents the formation energy.

$$E_f = E_{complex} - E_A - E_B \quad (5)$$

For the SrCoO_3 /graphene interface, the total energy of pure SrCoO_3 and pure graphene were calculated using the converged values for the kinetic energy cutoff and k-point grids. In this case, $E_{complex}$ represents the total energy of the interface. E_A represents the total energy of $1 \times 1 \times 2$ SrCoO_3 , and E_B represents the total energy of 2×2 graphene. The formalism is displayed in Eq. (6).

$$E_f = E_{complex} - 2 \times E_{\text{SrCoO}_3} - 4 \times E_{\text{graphene}} \quad (6)$$

In order to determine the formation energy of strontium cobaltite with vacancies, the total energy of oxygen gas was first calculated. $E_{complex}$ represents the formation energy of the complex with either one or two V_O . E_A is the total energy of $2 \times 2 \times 1$ SrCoO_3 . E_B is equal to n multiplied by the total energy of one oxygen atom, where n is the number of vacancies. The equation for the defect formation energy of the vacancy calculations can be found in Eq. (7).

$$E_f = E_{complex} - 4 \times E_{\text{SrCoO}_3} + n \times E_{\text{O}_2}/2 \quad (7)$$

To obtain the formation energy of doped SrCoO_3 , the total energies of the dopants and cobalt were calculated, along with the total energy of pure SrCoO_3 . $E_{complex}$ represents the total energy of the doped compound, which was calculated using the converged kinetic energy cutoff, Monkhorst-Pack k-point grids, and relaxed lattice constants. As the dopant is being substituted for a cobalt atom, we add the total energy of the cobalt atom and subtract the total energy of the dopant atom. Eq. (8) shows the formalism for the formation energy of the doping calculations.

$$E_f = E_{complex} - 4 \times E_{SrCoO_3} + E_{Co} - E_{dopant} \quad (8)$$

III. RESULTS AND DISCUSSION

In this section, we use DFT calculations to analyze the electronic and structural properties of an SrCoO₃/graphene interface, oxygen vacancies, and doping calculations as they apply to supercapacitor performance.

A. Interface

Previous studies have suggested that graphene has the potential to improve supercapacitor performance. Yang et al⁸, for example, has demonstrated that creating a Co₃O₄/graphene interface increased the energy density dramatically from 32 W h/kg to 43.1 W h/kg. Lang et al.¹⁷ also suggested that a perovskite/graphene interface has the potential to further increase the conductivity and stability of this material. Therefore, our goal is to theoretically study a perovskite/graphene interface to understand why graphene improves perovskite performance for supercapacitors.

An SrCoO₃/graphene interface was formed by $1 \times 1 \times 2$ SrCoO₃ and 2×2 graphene. The lattice parameters of the relaxed SrCoO₃ were used for the interface calculations. In lieu of relaxation, the optimal layer distance d between the perovskite and graphene was determined by incrementally increasing d by 0.5 Bohr and calculating the total energy. The layer distance with the lowest total energy was 5.5 Bohr, so this structure was used for DOS and formation energy calculations. We conclude that this value is reasonable because the graphene layer distance is around 6.6 Bohr³².

The lattice constants of the relaxed compounds are displayed in table III. The percentage error between the relaxed lattice constants and the published theoretical and experimental lattice constants for SrCoO₃ is always less than 1%. Furthermore, the relaxed lattice constants for graphene calculations fall within the range indicated by Girit et al³³, indicating that our relaxation calculations are reliable for both SrCoO₃ and graphene.

TABLE III: Relaxed Lattice Constants of SrCoO₃ and graphene

Compounds	Calculation Method	a (Bohr)	b (Bohr)	c (Bohr)
SrCoO ₃	GGA (this study)	7.21	7.21	7.21
	Experiment ³⁴	7.28	7.28	7.28
	GGA ²⁰	7.19	7.19	7.19
Graphene	GGA(this study)	4.62	4.62	
	Experiment ³³	4.35 - 4.72	4.35 - 4.72	
	GGA ³⁵	4.62	4.62	

To calculate the formation energy of the SrCoO₃/graphene interface, the total energy of pure SrCoO₃ and pure graphene were first calculated using the relaxed lattice constants given in Table III and the converged kinetic energy cutoff and Monkhorst-Pack k-point grids given in Table II. The formalism displayed in Eq. (6) was then applied to calculate the formation energy of the interface, which is 1.3 eV. Previous theoretical studies such as Hussain et al³⁶ have studied interactions between transition metal oxides (TMOs) and graphene for supercapacitor applications and determined the formation energy of CuO/graphene as 0.3 eV and FeO/graphene as 3.7 eV. Since the formation energy of the SrCoO₃/graphene interface falls between these two values, it can be concluded that the formation energy for this interface is reasonable and that the interface is relatively stable.

The charge transfer between graphene and SrCoO₃ was calculated in order to determine the areas of charge accumulation and charge depletion. To calculate the charge transfer, the converged charge density of the interface, pure SrCoO₃, and pure graphene were first obtained using the total energy calculations. The charge density of pure SrCoO₃ and pure graphene were then subtracted from the charge density of the interface to obtain the charge transfer. The resulting isosurface is displayed in Figure 2, and the isovalue used was 0.002 electrons/Bohr³. As shown in the figure, red regions indicate charge accumulation and blue areas indicate charge depletion.

The charge transfer could be caused by the strong hybridization of the C 2*p*, Sr 3*d*, Co 3*d*, and O 2*p* orbitals. Figure 2 (a) clearly shows that the oxygen atoms facilitate the charge transfer through the interface. Charge is transported away from the carbon atoms towards SrCoO₃ through the oxygen atoms. These results are similar to those obtained by Hussain



FIG. 2: (a) Side and (b) top views of isosurface for the interface. Red regions represent charge accumulation, and blue regions represent charge depletion. The blue atoms are Sr, the red atoms are O, the gray atoms are Co, and the yellow atoms are C. The isovalue used was 0.002 electrons/Bohr³.

et al³⁶ and Xiong et al¹⁰, where the oxygen exhibits weak accumulation of charge and acts as a conducting channel. Figure 2 (b) indicates that there is also accumulation of charge on the graphene layer, confirming the conductivity of the interface as a whole. It has been suggested by Lang et al¹⁷ that SrCoO₃ has the potential to prevent the agglomeration of graphene sheets through homogeneous dispersion. Due to this, it is possible that graphene not only increases the conductivity of the interface as a whole, but also can provide a buffer to accommodate the expansion and contraction of the cluster structure during charge/discharge cycles³⁶.

The total DOS (TDOS) and projected DOS (PDOS) were calculated for the SrCoO₃/graphene interface to analyze the contribution of the Sr 3*d*, Co 3*d*, O 2*p*, and

C 2*p* orbitals to the conduction process. The TDOS of pure SrCoO₃ is displayed in Figure 3 (a), and the TDOS of the SrCoO₃/graphene interface can be found in Figure 3 (b). Compared to the TDOS of the pure perovskite, the interface calculation has more peaks in both the conduction and valence bands, indicating that the interface is more conductive overall than pure SrCoO₃. Figure 3 (b) shows no band gap, which is to be expected because of the metallic nature of the SrCoO₃/graphene interface. Furthermore, the non-zero states at and around the Fermi level indicate an overlap between the valence and conduction bands and show that the states are shifting away from the valence bands towards the conduction bands.

The PDOS of the interface was calculated and is displayed in Figure 3 (d), and the PDOS of the pure SrCoO₃ is shown in Figure 3 (c) for comparison. The increased presence of non-zero localized states at and around the Fermi level indicates the increased conductivity of this material. It is clearly evident that the PDOS plot has many sharp peaks and that peaks are present for every material used in the interface, so it can be said that SrCoO₃ and graphene contribute equally to the conductivity of the interface. The increased number of coinciding peaks indicates the strong hybridization between C 2*p*, O 2*p*, Co 3*d*, and Sr 3*d*. The PDOS of the composite system is similar to the DOS of Sr, Co, and O as plotted by earlier studies³⁷. Therefore, we can conclude that due to the relative stability and extremely high conductivity of this SrCoO₃/graphene interface, it has the potential to be an effective supercapacitor electrode.

B. Oxygen vacancies

A multitude of studies have concluded that inducing oxygen vacancies improves the conductivity of materials for supercapacitor applications^{8,12,38}. Cheng et al³⁹ specifically found that inducing oxygen vacancies in Co₃O₄ increased the specific capacitance of the complex material significantly. In the present study, we simulate one oxygen vacancy by removing one oxygen atom in a $2 \times 2 \times 1$ supercell; similarly, we induce two oxygen vacancies by taking out one oxygen and its nearest neighboring oxygen atom. We then calculate the formation energy, band structure, and PDOS of the supercell with one V_O and two V_O and compare the two with pure SrCoO₃.

Oxygen vacancies were first induced in a pure SrCoO₃ supercell of size $2 \times 2 \times 1$. After

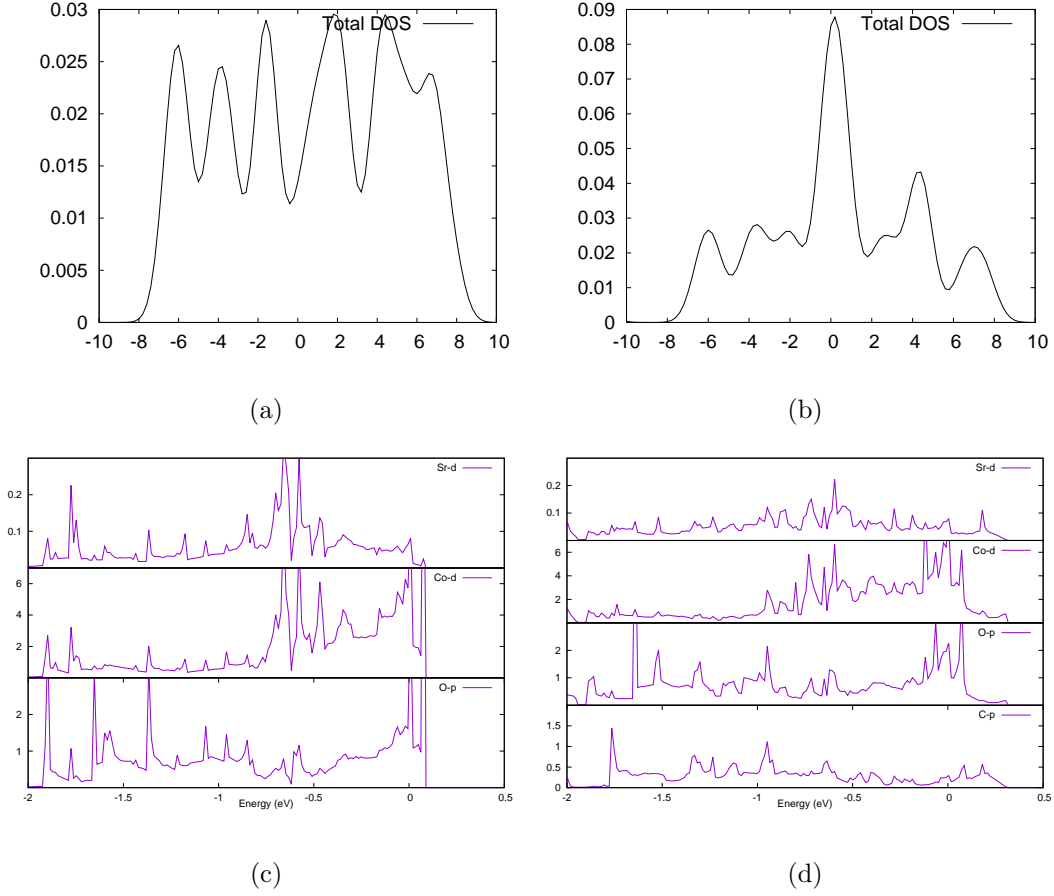


FIG. 3: TDOS of (a) pure SrCoO_3 and (b) the SrCoO_3 /graphene interface. (c) shows the PDOS of pure SrCoO_3 and (d) shows the PDOS of the SrCoO_3 /graphene interface. The increased number of states near the Fermi level for the interface in (b) and (d) indicates that it is extremely conductive due to the hybridization of the Sr $3d$, Co $3d$, O $2p$, and C $2p$.

TABLE IV: Relaxed lattice constants for SrCoO_3 supercell with oxygen vacancies

Number of vacancies	a (Bohr)	b (Bohr)	c (Bohr)
One	14.4	14.4	7.22
Two	14.5	14.5	7.23

the oxygen was removed, the structure was relaxed again and the band structure and the PDOS were calculated. To simulate two oxygen vacancies, an oxygen atom and its nearest neighbor were both taken out. Table IV shows that with two vacancies, the relaxed lattice constant increases slightly.

The defect formation energy of the complex structures was calculated. To do this, the total energy of pure SrCoO_3 was determined using the relaxed lattice constants in Table III and converged kinetic energy cutoff and Monkhorst-Pack k-point grids displayed in Table II. The formalism defined in Eq. (7) was then used to determine the defect formation energy of the oxygen vacancies. The formation energy of the complex with one oxygen vacancy is 2.75 eV, while the formation energy of the complex with two oxygen vacancies is 7.62 eV. Since a lower formation energy is indicative of a more stable compound, the complex with one oxygen vacancy is more stable than the complex with two oxygen vacancies. This is to be expected, as inducing vacancies disrupts the crystal structure and therefore decreases the stability of the system. Compared to other studies which have analyzed oxygen vacancies with transition metal oxides, the complex with one oxygen vacancy is relatively stable. Previous studies have shown that inducing an oxygen vacancy in TiO_2 results in a formation energy of around 2-5 eV⁴⁰. Since the formation energy of one oxygen vacancy is similar to this range, we conclude that the formation energies of these complexes are reasonable.

The fat-band structures of the one-vacancy complex and the two-vacancy complex were calculated and are displayed in Figure 4. The contributions by the oxygen 2*p* orbital are plotted in red, and it is evident that inducing oxygen vacancies increases the contributions of oxygen to the bands around the Fermi level. The oxygen 2*p* orbital contributes more to the two-vacancy complex than to the one-vacancy complex, demonstrating that the contributions of the oxygen 2*p* orbital increase as the number of vacancies increases. As expected, there is little to no band gap near the Fermi level, which indicates that the materials in question are metallic.

In order to yield further insights into the conductivity of the complexes with vacancies, TDOS and PDOS were calculated. To calculate the DOS, the total energy was determined using the converged kinetic energy cutoffs and Monkhorst-Pack k-point grids, as well as the relaxed lattice vectors shown in Table IV. The TDOS of the complexes can be found in Figure 5 (b) and (c). The total DOS of the pure SrCoO_3 is also shown in Figure 5 (a) for comparison. It is clearly evident from 5 (b) and 5 (c) that inducing oxygen vacancies improves the conductivity of the complex because of the increased number of peaks in the TDOS in figures 5(b) and (c). Figures 5 (b) and (c) show no band gap, which is to be expected because of the metallic nature of SrCoO_3 . In addition, the non-zero states at and around the Fermi level indicate an overlap between the valence and conduction bands and

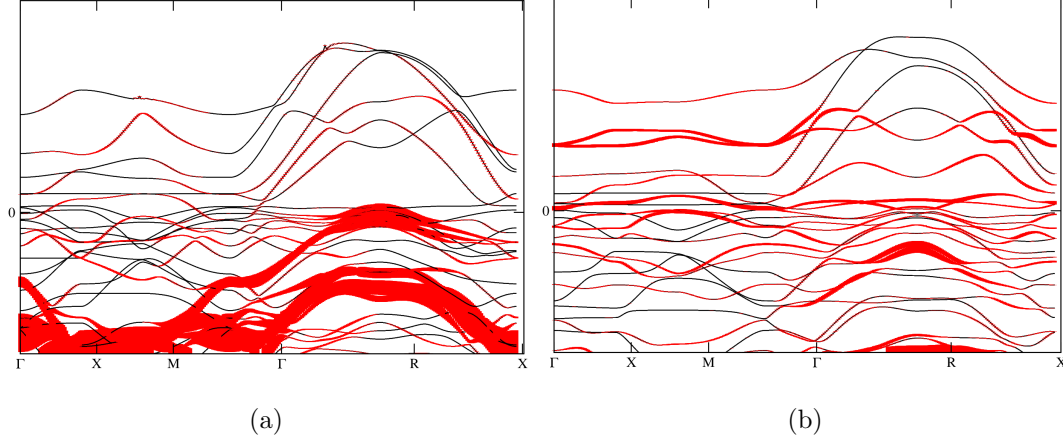


FIG. 4: Fat-band structure for an SrCoO_3 complex with (a) one oxygen vacancy and (b) two oxygen vacancies. The contributions of the oxygen 2p orbital are shown in red. The high symmetry k-points for the cubic structure were used and are: Γ (0, 0, 0), X(0, 0.5, 0), M(0.5, 0.5, 0.0), and R(0.5, 0.5, 0.5)

show that the states are shifting away from the valence bands towards the conduction bands.

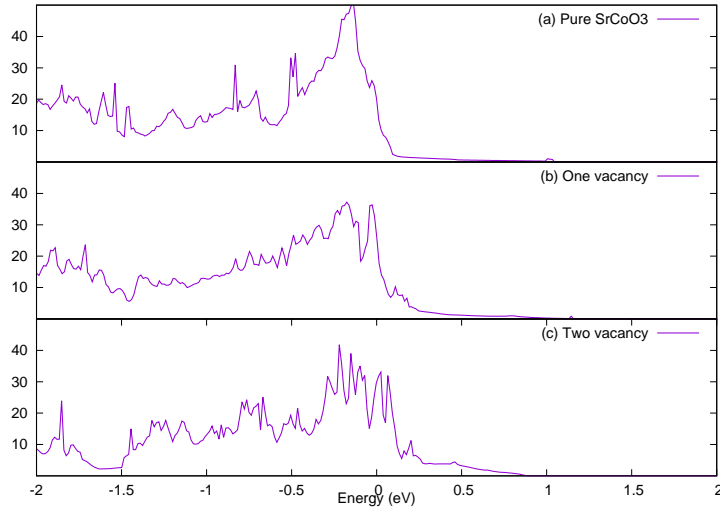


FIG. 5: Total DOS for (a) pure SrCoO_3 , (b) an SrCoO_3 complex with one vacancy, and (c) an SrCoO_3 complex with two vacancies. Since there is little to no band gap around the Fermi level, we can conclude that these materials are metallic.

The PDOS of the complexes were also calculated in order to determine the contributions of Sr 3d, Co 3d, and O 2p with vacancies to the conduction process. The PDOS reveals that vacancies increase the conductivity of SrCoO_3 tremendously, and there is also a

considerable increase in conductivity from one vacancy to two vacancies. Figures 6 (a) and (b) show that there are localized states at and around the Fermi level, indicating an increase in conductivity. In addition, peaks are present for all elements, indicating that Sr, Co, and O contribute equally to the conduction process. The non-zero states at the Fermi level show that there is an overlap between the valence and conduction band edges that reveals a shift away from the valence band (VB) toward conduction bands (CB). The increased number of states from one vacancy to two vacancies reveals the strong hybridization of the Sr $3d$, Co $3d$, and O $2p$ orbitals caused by the vacancy. Due to the increase in conductivity caused by vacancies and their relative stability, we conclude that inducing oxygen vacancies in SrCoO_3 increase its performance as a supercapacitor electrode.

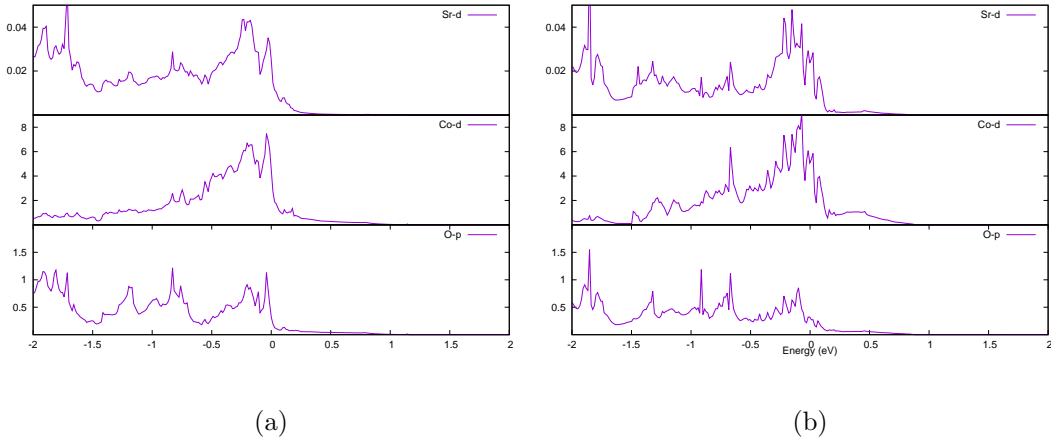


FIG. 6: PDOS for an SrCoO_3 supercell with (a) one oxygen vacancy and (b) two oxygen vacancies. The PDOS of the Sr $2p$ orbital is shown at the top, then the Co $3d$ orbital, and then O $2p$ orbital is displayed.

The converged charge density was calculated for both one V_O and 2 V_O and the results are displayed in figure 7. The charge density was obtained by calculating the total energy of the complex using the kinetic energy cutoffs and k-point grids of pure SrCoO_3 and the relaxed lattice constants of the complex. The isovalue used was 0.03 electrons/Bohr³. Figure 7 (a) shows that the charge accumulation is centered around the vacancies, which is well in agreement with published studies⁸. Similarly, Figure 7(b) shows two concentrated areas of charge accumulation caused by the two vacancies in the structure. This accumulation is most likely caused by the increased electron delocalization of the surrounding Sr and Co atoms as a result of the oxygen vacancy. In addition, the charge accumulation could also

have been caused by the strong hybridization of the Sr $3d$, Co $3d$, and O $2p$ orbitals, which supports the PDOS calculations shown in Figure 6.

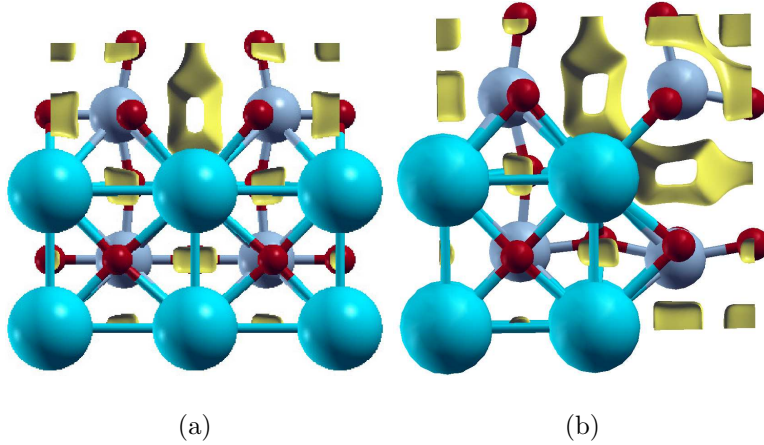


FIG. 7: Isosurface diagrams for SrCoO_3 complexes containing (a) one oxygen vacancy and (b) two oxygen vacancies. The yellow areas indicate charge accumulation. The blue atoms are Sr, the red atoms are O, and the gray atoms represent Co.

C. Doping

We choose Mo, V, P, and Nb as dopants to investigate how they increase the OER of SrCoO_3 . We also study whether nonmetallic dopants can achieve the same level of conductivity and stability as the metallic dopants.

To achieve 25% substitutional doping at the B-site of SrCoO_3 , a $2 \times 2 \times 1$ supercell was used, in which one cobalt atom was replaced with the dopant. The complex was then relaxed and the band structure, PDOS, and formation energy were calculated for each dopant and compared to determine the most effective dopant.

Once a cobalt atom was substituted for one of the dopants, the resulting structure was relaxed again. The fully relaxed structure of the complex remained cubic when the dopant was Mo, V, or Nb, which confirms experimental results, as these dopants do not alter the basic structure of SrCoO_3 . For P-doped SrCoO_3 , however, the structure was altered from cubic to tetragonal, which supports the experimental results found by Zhu et al¹⁵. Table V displays the relaxed lattice constants of each complex. The atomic structure is displayed in Figure 8.

TABLE V: Relaxed lattice constants of doped SrCoO₃

Compound	a (Bohr)	b (Bohr)	c (Bohr)
Mo-doped SrCoO ₃	14.64	14.64	7.32
V-doped SrCoO ₃	14.52	14.52	7.26
P-doped SrCoO ₃	14.77	14.77	7.39
Nb-doped SrCoO ₃	14.69	14.69	7.34

TABLE VI: Formation energy for doped SrCoO₃ with different dopants

Compound	Formation Energy (eV)
Mo-doped SrCoO ₃	-7.46
V-doped SrCoO ₃	-7.88
P-doped SrCoO ₃	-6.07
Nb-doped SrCoO ₃	-9.89

The formation energy for all dopants was calculated. To do this, the total energy was calculated for the doped complex, pure SrCoO₃, pure cobalt, and the pure dopant using the converged kinetic energy cutoffs, Monkhorst-Pack k-point grids, and relaxed lattice vectors. The formalism displayed in Eq. (8) was used to calculate the formation energy of the complex, and the results are displayed in Table VI. It has been well-documented by Hussain et al⁴¹ and others that a lower formation energy is an indicator of stability of a structure. These DFT calculations reveal that niobium-doped SrCoO₃ has the lowest formation energy of -9.89 eV, indicating that it is the most stable compound of the four dopants. All of the formation energies are negative, which indicates that exothermic reactions are taking place. This further confirms that all of the complexes are stable as they do not gain heat during the doping reaction.

The band structure of all four dopants reveals that there is little to no band gap around the Fermi level as expected, which reveals the metallic behavior of these systems. The contributions of the dopant to the band structure is shown in Figure 9 in the form of

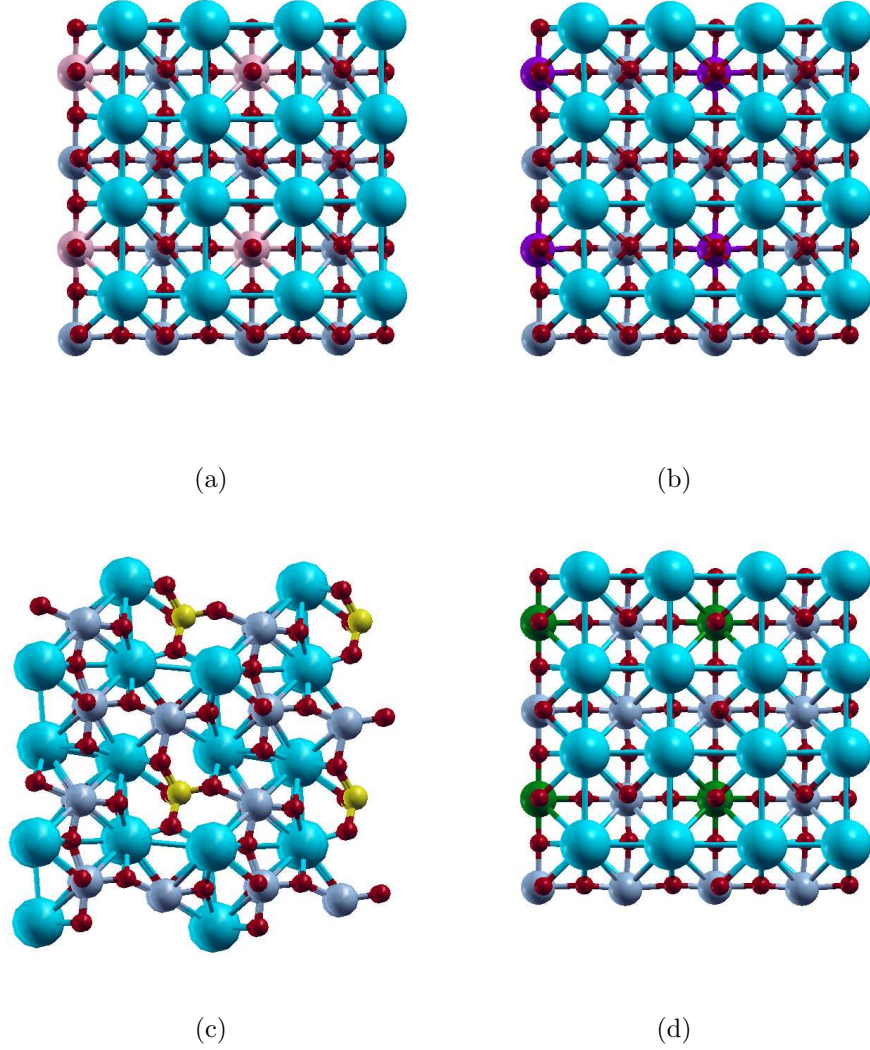


FIG. 8: Atomic structure for (a) Mo-doped SrCoO_3 , (b) V-doped SrCoO_3 , (c) P-doped SrCoO_3 , (d) Nb-doped SrCoO_3 . The blue atoms represent Sr, the gray atoms represent Co, the red atoms represent O, the pink atoms represent Mo, the purple atoms represent V, the yellow atoms represent P, and the green atoms represent Nb.

fat-bands in order to analyze how the dopant affects the band structure. Figure 9 shows that niobium, vanadium and molybdenum substantially affect the band structure of the complex, while Phosphorus does so to a lesser extent because of the lack of a d orbital. This reveals that metallic dopants are more effective than non-metallic dopants for supercapacitor applications. Therefore, we can conclude that metallic dopants are more effective than nonmetallic dopants for supercapacitor electrodes.

The total DOS was analyzed for further insight into the conductive behavior of the

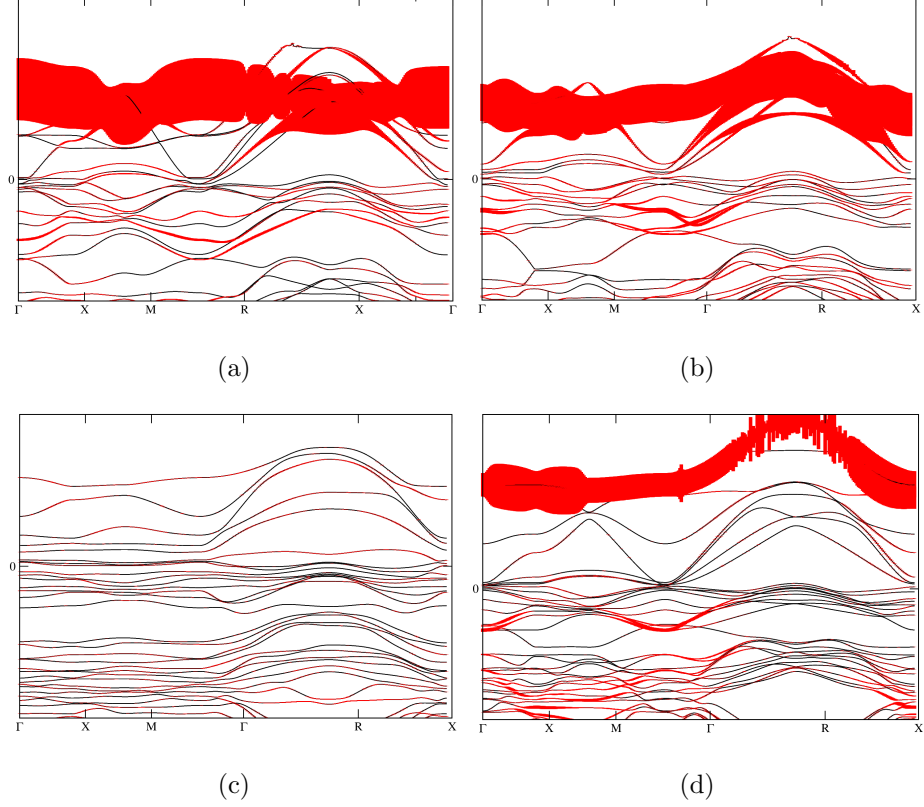


FIG. 9: Fat-band structure for (a) Mo-doped SrCoO_3 , (b) V-doped SrCoO_3 , (c) P-doped SrCoO_3 , (d) Nb-doped SrCoO_3 . The red areas indicate the contribution of dopants to the band structure. The high symmetry k-points for simple cubic structures were chosen to most effectively sample the First Brillouin Zone and are Γ (0, 0, 0), X(0, 0.5, 0), M(0.5, 0.5, 0.0), and R(0.5, 0.5, 0.5)

dopants and how they affect the total conductivity of the complex. The TDOS was calculated by first calculating the total energy using the converged kinetic energy cutoffs and k-point grids, along with the relaxed lattice constants of the complexes, and is plotted in Figure 10. The total DOS of pure SrCoO_3 is also plotted in Figure 10 (e) for comparison.

Analysis of the TDOS and PDOS reveals the conductive behavior of doped SrCoO_3 . Figure 11 reveals that all four dopants increase the conductivity substantively, as shown by the non-zero localized states around the Fermi level. However, it is clear that phosphorus is the least conductive dopant because the values of the states are considerably lower for phosphorus TDOS than for any of the other dopants. The PDOS shows that Mo and V achieve similar results as dopants, with an increased conductivity shown by the $3p$ -orbital for Sr, the d -orbital for Cobalt, the $2p$ -orbital for Oxygen, and the d -orbital for the dopants. It can be said that the increased number of peaks shown in the PDOS are a result of the

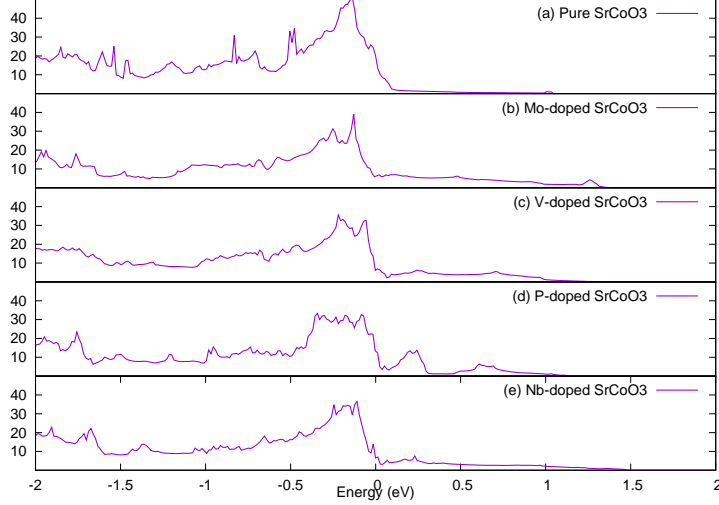


FIG. 10: TDOS for all of the doped compounds. Figure (a) shows the TDOS of pure SrCoO_3 , (b) shows the TDOS for Mo-doped SrCoO_3 , (c) shows the TDOS for V-doped SrCoO_3 , (d) shows the TDOS for P-doped SrCoO_3 , and (e) shows the TDOS for Nb-doped SrCoO_3 .

hybridization of the Sr $3d$, Co $3d$, O $2p$ and the $3d$ orbitals of the metallic dopants. It is evident that Niobium is by far the best dopant for SrCoO_3 , as the states are much higher and there are more states for Nb-doped SrCoO_3 than any other dopant. For all four dopants, it is evident from the nonzero states around the fermi level that there is an overlap between the conduction bands (CB) and valence bands (VB) and that the states shift away from the CB towards the VB. For all of the dopants, there are states around the Fermi level for all four elements (Sr, Co, O, and the dopant), showing that all of the elements contribute equally to the conduction process. Taken together, the formation energy, band structure and PDOS reveal that while all of the dopants studied increase the compound's conductivity, niobium is the best dopant due to its higher stability (as given by the lower formation energy) and its greater conductivity (as shown by the PDOS and the band structure). Furthermore, the PDOS and fat-band structure reveal that phosphorus is not as effective as the rest of the dopants. This shows that metallic dopants should be used to improve supercapacitor performance. In addition, we have discovered that vanadium is a promising new dopant for SrCoO_3 as anion-intercalation-type supercapacitor electrode.

Our findings suggest the viability of a novel SrCoO_3 /graphene interface for supercapacitor applications. Previous studies involving TMO/graphene interfacial structures have

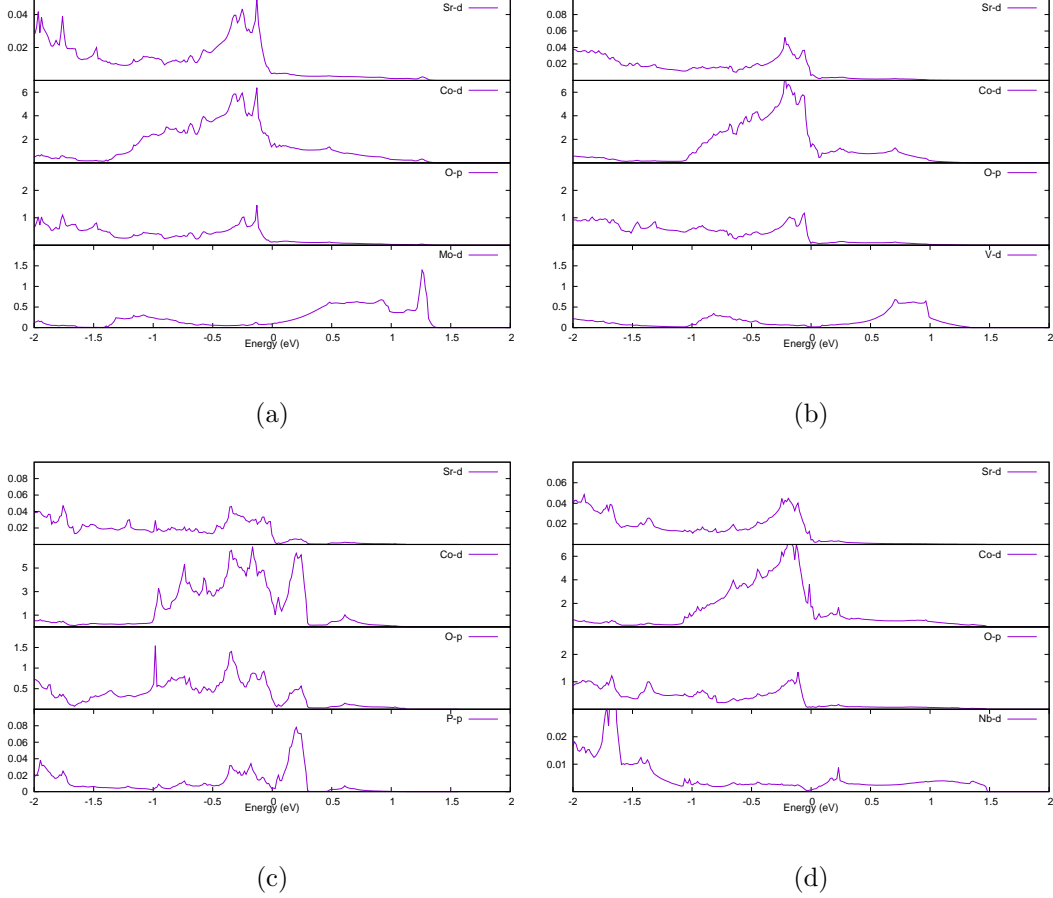


FIG. 11: PDOS for all of the doped compounds. For O, the 2 p orbital was analyzed, and the 3 d orbital was plotted for Co and Sr. For Molybdenum, shown in (a), the 4 d orbital was plotted, and for Vanadium, shown in (b), the 3 d orbital was plotted. Phosphorus does not have a d orbital, so the 2 p orbital was analyzed instead in (c). The 4 d orbital was plotted for Niobium in (d).

suggested that oxygen acts as a conducting channel between graphene and the cluster structure^{10,36}, which increases the conductivity of the interface, which supports our electronic charge density calculations. Compared to FeO/graphene, which has a formation energy of 3.7 eV³⁶, and MnO₂/graphene, which has a formation energy of 5.5 eV¹⁰, we find that our SrCoO₃/graphene interface is relatively stable with a formation energy of only 1.3 eV. Our PDOS calculations are also supported by Xiong et al¹⁰ and Hussain et al³⁶, who report that TMO/graphene interfacial structures exhibit more peaks that coincide with each other due to the strong hybridization of the Sr 3*d*, Co 3*d*, C 2*p* and O 2*p* orbitals.

We also theoretically verify that inducing oxygen vacancies in SrCoO₃ increases the conductivity of SrCoO₃ due to the strong hybridization of the Sr 3*d*, Co 3*d*, and O 2*p* orbitals.

Yang et al⁸ and Cheng et al³⁹, among others, have concluded that inducing oxygen vacancies in TMOs decreases the stability but increases the conductivity of the material, which we confirm through formation energy and PDOS calculations. In addition, previous studies have also found that inducing oxygen vacancies results in charge accumulation around the vacancy due to electron delocalization in the surrounding atoms^{39,42} this is supported by our electronic charge density calculations.

Furthermore, we find that doping at the B-site with Mo, V, P, and Nb increases the stability of this material and also improves the conductivity of SrCoO₃. Mo has been previously studied as a dopant for SrCoO₃ in both supercapacitor applications⁵ and for solid oxide fuel cells¹⁹ due to its OER-enhancing properties, which make this perovskite more conductive. We confirm this conductive behavior through fat-band calculations, which reveal Molybdenum's increased contribution to the band structure of Mo-doped SrCoO₃. Our PDOS calculations show that Mo-doped SrCoO₃ results in strong hybridization of Mo *d*, Sr *d*, Co *d*, and O *p* orbitals. Zhu et al¹⁵ studied the effect of P-doping on SrCoO₃ as an OER catalyst and concluded that phosphorus significantly changes the structure of SrCoO₃, which supports our relaxation calculations. Although they concluded that this resulted in a more stable compound, we find that the other dopants increase the stability of SrCoO₃ to a much greater extent. However, previous studies have concluded that a small amount of doping at the B-site increases the stability of SrCoO₃^{6,43}. We confirm this as doping with any of the four dopants resulted in a complex with a very low formation energy, indicating the stability. Li et al²⁹ found that doping SrCoO₃ with niobium resulted in a very high energy density and also prolonged cycling life, which supports our conclusion that Niobium is the best dopant of the four dopants because it significantly increases the stability of this compound and also contributes tremendously to the conductivity. To the best of our knowledge, vanadium and phosphorus have not been studied as dopants for SrCoO₃ for supercapacitor applications. Nevertheless, our conclusions that these compounds enhance the OER of SrCoO₃ and also increase the stability are supported by the findings of Zhu et al¹⁵ and Guo et al⁹. However, we find that phosphorus is the least effective dopant due to its lack of a *d* orbital, which reveals that metallic dopants are more effective for anion-intercalation-type supercapacitors. Therefore, we can conclude that vanadium and to a lesser degree phosphorus are both novel, promising dopants for supercapacitor applications.

IV. CONCLUSION

In this study, we use Density Functional Theory to explore various methods the performance of the perovskite SrCoO_3 for supercapacitor applications. We systematically study electronic structure properties and formation energies.

An SrCoO_3 /graphene interface was studied to analyze how graphene contributes to the performance of SrCoO_3 as a supercapacitor electrode. The formation energy of the interface was 1.3 eV, which is relatively stable compared to other TMO/graphene interface structures. Both DOS calculations and electronic charge density indicate that the interface is extremely conductive.

Oxygen vacancies were induced to determine the mechanism by which vacancies improve the conductivity of SrCoO_3 . The defect formation energy of one oxygen vacancy is 2.5 eV, which is comparable to other studies which have induced oxygen vacancies in TMOs. Fat-band structures reveal that vacancies cause the oxygen $2p$ orbital to contribute more to the band structure, and DOS calculations support this conclusion. The PDOS calculations reveal that oxygen vacancies cause a dramatic increase in the conductivity of the material.

We also doped SrCoO_3 with four different dopants, Mo, V, P, and Nb, at 25% concentrations at the B-site by replacing one Co atom with one dopant atom. We evaluated the performance of each dopant by calculating the formation energy, TDOS, PDOS, and fat-band structure. All calculations show that all four dopants improve SrCoO_3 performance drastically. Niobium is the best dopant of the four because it had the lowest formation energy of -9.89 eV. In addition, Niobium contributed the most to the fat-band structure of any of the four dopants and is the most conductive as shown by PDOS. Vanadium is also a promising new dopant for anion-intercalation-type supercapacitor electrodes.

Therefore, we conclude that a graphene interface, oxygen vacancies, and doping can all improve the performance of SrCoO_3 as an anion-intercalation type supercapacitor electrode to different extents.

-
- ¹ L. H. Saw, H. M. Poon, W. T. Chong, C.-T. Wang, M. C. Yew, M. K. Yew, and T. C. Ng, *Energy Procedia* **158**, 2750 (2019).
- ² W. Wei, X. Cui, W. Chen, and D. G. Ivey, *Chemical society reviews* **40**, 1697 (2011).
- ³ M. Horn, J. MacLeod, M. Liu, J. Webb, and N. Motta, *Economic Analysis and Policy* **61**, 93 (2019).
- ⁴ G. Wang, L. Zhang, and J. Zhang, *Chemical Society Reviews* **41**, 797 (2012).
- ⁵ A. K. Tomar, G. Singh, and R. K. Sharma, *ChemSusChem* **11**, 4123 (2018).
- ⁶ G. George, S. L. Jackson, C. Q. Luo, D. Fang, D. Luo, D. Hu, J. Wen, and Z. Luo, *Ceramics International* **44**, 21982 (2018).
- ⁷ S. Yang, Z. Han, J. Sun, X. Yang, X. Hu, C. Li, and B. Cao, *Electrochimica Acta* **268**, 20 (2018).
- ⁸ S. Yang, Y. Liu, Y. Hao, X. Yang, W. A. Goddard III, X. L. Zhang, and B. Cao, *Advanced Science* **5**, 1700659 (2018).
- ⁹ M. Guo, J. Balamurugan, N. H. Kim, and J. H. Lee, *Applied Catalysis B: Environmental* **239**, 290 (2018).
- ¹⁰ G. Xiong, K. Hembram, R. Reifemberger, and T. S. Fisher, *Journal of Power Sources* **227**, 254 (2013).
- ¹¹ S. Nagarani, G. Sasikala, K. Satheesh, M. Yuvaraj, and R. Jayavel, *Journal of Materials Science: Materials in Electronics* **29**, 11738 (2018).
- ¹² Y. Wang, T. Zhou, K. Jiang, P. Da, Z. Peng, J. Tang, B. Kong, W.-B. Cai, Z. Yang, and G. Zheng, *Advanced Energy Materials* **4**, 1400696 (2014).
- ¹³ Y. Liu, J. Dinh, M. O. Tade, and Z. Shao, *ACS applied materials & interfaces* **8**, 23774 (2016).
- ¹⁴ V. Ozolins, F. Zhou, and M. Asta, *Accounts of chemical research* **46**, 1084 (2013).
- ¹⁵ Y. Zhu, W. Zhou, J. Sunarso, Y. Zhong, and Z. Shao, *Advanced Functional Materials* **26**, 5862 (2016).
- ¹⁶ Y. Liu, Z. Wang, J.-P. M. Veder, Z. Xu, Y. Zhong, W. Zhou, M. O. Tade, S. Wang, and Z. Shao, *Advanced Energy Materials* **8**, 1702604 (2018).
- ¹⁷ X. Lang, H. Mo, X. Hu, and H. Tian, *Dalton Transactions* **46**, 13720 (2017).
- ¹⁸ H. Mo, H. Nan, X. Lang, S. Liu, L. Qiao, X. Hu, and H. Tian, *Ceramics International* **44**, 9733

- (2018).
- ¹⁹ A. Aguadero, D. Pérez-Coll, J. Alonso, S. Skinner, and J. Kilner, *Chemistry of Materials* **24**, 2655 (2012).
 - ²⁰ T. Jia, Z. Zeng, H. Lin, Y. Duan, and P. Ohodnicki, *RSC Advances* **7**, 38798 (2017).
 - ²¹ F. Calle-Vallejo, O. A. Díaz-Morales, M. J. Kolb, and M. T. Koper, *ACS Catalysis* **5**, 869 (2015).
 - ²² X. Gonze, B. Amadon, P.-M. Anglade, J.-M. Beuken, F. Bottin, P. Boulanger, F. Bruneval, D. Caliste, R. Caracas, M. Côté, *et al.*, *Computer Physics Communications* **180**, 2582 (2009).
 - ²³ J. P. Perdew, K. Burke, and M. Ernzerhof, *Physical review letters* **77**, 3865 (1996).
 - ²⁴ P. E. Blöchl, *Physical review B* **50**, 17953 (1994).
 - ²⁵ N. Holzwarth, A. Tackett, and G. Matthews, *Computer Physics Communications* **135**, 329 (2001).
 - ²⁶ C. T. Alexander, J. T. Mefford, J. Saunders, R. P. Forslund, K. P. Johnston, and K. J. Stevenson, *ACS applied materials & interfaces* **11**, 5084 (2019).
 - ²⁷ T. Zhai, S. Xie, M. Yu, P. Fang, C. Liang, X. Lu, and Y. Tong, *Nano Energy* **8**, 255 (2014).
 - ²⁸ K. Xiang, Z. Xu, T. Qu, Z. Tian, Y. Zhang, Y. Wang, M. Xie, X. Guo, W. Ding, and X. Guo, *Chemical Communications* **53**, 12410 (2017).
 - ²⁹ M. Li, M. Zhao, F. Li, W. Zhou, V. K. Peterson, X. Xu, Z. Shao, I. Gentle, and Z. Zhu, *Nature communications* **8**, 13990 (2017).
 - ³⁰ D. Yang, *Journal of Power Sources* **228**, 89 (2013).
 - ³¹ W. Setyawan and S. Curtarolo, *Computational materials science* **49**, 299 (2010).
 - ³² A. Affoune, B. Prasad, H. Sato, T. Enoki, Y. Kaburagi, and Y. Hishiyama, *Chemical Physics Letters* **348**, 17 (2001).
 - ³³ Ç. Ö. Girit, J. C. Meyer, R. Erni, M. D. Rossell, C. Kisielowski, L. Yang, C.-H. Park, M. Crommie, M. L. Cohen, S. G. Louie, *et al.*, *science* **323**, 1705 (2009).
 - ³⁴ Y. Wang, L. Yu, J. Wang, L. Chen, W. Gao, X. Du, and L. Biao, *Materials Letters* **75**, 39 (2012).
 - ³⁵ G. Giovannetti, P. Khomyakov, G. Brocks, V. v. Karpan, J. Van den Brink, and P. J. Kelly, *Physical review letters* **101**, 026803 (2008).
 - ³⁶ F. Hussain, M. Imran, U. Rasheed, R. A. Khalil, A. M. Rana, F. Kousar, M. A. Javid, and S. Hayat, *Journal of Electronic Materials* **48**, 2343 (2019).

- ³⁷ K. Van Benthem, C. Elsässer, and R. French, *Journal of Applied Physics* **90**, 6156 (2001).
- ³⁸ K. Xiang, Z. Xu, T. Qu, Z. Tian, Y. Zhang, Y. Wang, M. Xie, X. Guo, W. Ding, and X. Guo, *Chemical Communications* **53**, 12410 (2017).
- ³⁹ G. Cheng, T. Kou, J. Zhang, C. Si, H. Gao, and Z. Zhang, *Nano Energy* **38**, 155 (2017).
- ⁴⁰ S. Na-Phattalung, M. F. Smith, K. Kim, M.-H. Du, S.-H. Wei, S. Zhang, and S. Limpijumnong, *Physical Review B* **73**, 125205 (2006).
- ⁴¹ F. Hussain, M. Imran, A. M. Rana, R. A. Khalil, E. A. Khera, S. Kiran, M. A. Javid, M. A. Sattar, and M. Ismail, *Applied Nanoscience* **8**, 839 (2018).
- ⁴² F. Cheng, T. Zhang, Y. Zhang, J. Du, X. Han, and J. Chen, *Angewandte Chemie International Edition* **52**, 2474 (2013).
- ⁴³ H.-s. Nan, X.-y. Hu, and H.-w. Tian, *Materials Science in Semiconductor Processing* **94**, 35 (2019).